Enhanced optical fiber fabrication via the MCVD process incorporating pre-synthesized ZrO2 nanoparticles

Lilia Sennoun, Ileana Florea, François Orange, Michèle Ude, Peter Hesemann, Ahmad Mehdi, Wilfried Blanc

Optical Materials 164 (2025) 117015

Contents lists available at ScienceDirect

Optical Materials

journal homepage: www.elsevier.com/locate/optmat

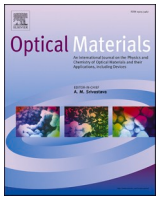

Enhanced optical fiber fabrication via the MCVD process incorporating pre-synthesized ZrO_2 nanoparticles

Lilia Sennoun [a], Ileana Florea [b], François Orange [c], Michele Ude [d], Peter Hesemann [a], Ahmad Mehdi [a], Wilfried Blanc [d,*]

[a] Université de Montpellier, CNRS, ICGM, France
[b] Université Côte D'Azur, CNRS, CRHEA, Rue B. Grégory, 06560, Valbonne, France
[c] Université Côte D'Azur, Centre Commun de Microscopie Appliquée (CCMA), 06108, Nice, France
[d] Université Côte D'Azur, CNRS, INPHYNI, France

ARTICLE INFO

Keywords:
Optical fiber
ZrO_2
Nanocrystals
MCVD
STEM
EDS
SEM

ABSTRACT

Nanoparticle-doped optical fibers have experienced significant advancements in recent years, driven by their numerous applications. Nanoparticles (NPs) enable the isolation of luminescent ions from the silica matrix allowing precise engineering of luminescence properties. Additionally, light scattering induced by nanoparticles can also be exploited to develop sensors. The effectiveness of these applications relies on the ability to control the nanoparticle characteristics within the fiber. This study highlights the use of pre-synthesized zirconium oxide (ZrO_2) nanocrystals as dopant with a particular focus on their characterization at every stage of the manufacturing process. The findings highlight the survival of ZrO_2 nanocrystals throughout the entire process, from the preform to the as-drawn fiber, demonstrating the robustness and potential of this approach.

1. Introduction

Silica (SiO_2) has long been the ideal host matrix for the fabrication of optical fibers, owing to its outstanding intrinsic properties such as high transparency over a wide wavelength range, thermal and chemical stability, high durability, and good compatibility with common optical components [1]. However, pure silica glass reveals certain limitations which could be detrimental for new applications. For instance, the high energy of phonon in silica glass reduces the quantum yield of rare-earth ions, affecting their photoluminescence [2]. Furthermore, the ultra-high transparency of silica glass leads to a small backscattered signal of interest for sensors [3].

In order to overcome these limitations and to avoid the need of utilizing alternative glass compositions, one potential approach is to form glass-ceramics, a glassy matrix containing crystalline particles whose composition differs from that of the host matrix [4].

To illustrate this approach, the work of Professor Giancarlo Righini, that we celebrate in this special issue, is strongly inspiring. Indeed, during the last 35 years, Professor Giancarlo Righini was strongly involved in many studies aiming at improving the rare-earth ions luminescent properties in silica-based glass-ceramics waveguides. In 1989, he started to study the nonlinear optical properties of glass containing semi-conductor nanoparticles such as Cd(Se,S) [5–7]. Twenty years later, he was interested in the formation of silica-based glass--ceramics containing oxide nanocrystals, in particular SnO_2 and HfO_2 [8–11]. The aim was to isolate the rare-earth ions (Er^{3+}, Yb^{3+}, Tb^{3+}) within the nanocrystals to improve their luminescence properties.

Over the last years, this strategy has been applied to optical fibers too [12,13]. Depending on the applications, the requirements on the characteristics of the nanoparticles are different. For laser technology, small nanoparticles (~10 nm) are of interest to minimize optical loss induced by light scattering [14]. On the contrary, sensors are based on light scattering so larger nanoparticles are required to enhance their performance [15].

Numerous techniques have been adopted to create these nanoparticles within the matrix, such as post heat-treatment of optical fibers [14] or *in situ* formation and growth of nanoparticles in the preform via phase separation mechanisms [16]. In both cases, a number of parameters, including the temperature selected, the treatment duration, and the concentration of the phase-separating element in the doping

This article is part of a special issue entitled: 80th birthday of Giancarlo C. Righini published in Optical Materials.

* Corresponding author.
E-mail address: wilfried.blanc@univ-cotedazur.fr (W. Blanc).

https://doi.org/10.1016/j.optmat.2025.117015
Received 3 March 2025; Received in revised form 28 March 2025; Accepted 31 March 2025
Available online 4 April 2025

solution, affect nucleation and particle growth. Moreover, the drawing step can also alter the characteristics of the nanoparticles [17,18]. Very small nanoparticles can be produced by high-temperature fiber drawing (2050 °C), whereas lower temperature (1850 °C) favors the formation of elongated and fragmented particles [19].

A more convenient route would be to incorporate pre-synthesized nanoparticles during the fabrication of the preform by using the Modified Chemical Vapor Deposition (MCVD) process and the solution doping step. However, a key challenge lies in preserving the integrity of these nanoparticles against the corrosive action of the host matrix at elevated temperature (typically 2000 °C). It has been shown recently that $YbPO_4$ nanocrystals, introduced into a silica preform, survive until drawn into optical fibers, retaining their original composition and structure [20]. On the contrary, $Y_3Al_5O_{12}$ (YAG) nanocrystals react to form YPO_4 nanocrystals if the porous layer contains phosphorous, or amorphous Y_2O_3–Al_2O_3–SiO_2 (YAS) nanoparticles if there is no phosphorous in the porous layer [21,22]. Fluoride nanoparticles, such as LaF_3:Tm^{3+}, undergo transformations during the fabrication process due to the high reactivity of fluoride ions with silica. This reaction leads to the formation of the gaseous species SiF_4, causing fluorine evaporation and resulting in the conversion of LaF_3 into La-silicate nanoparticles [23]. These results indicate that the study of the survival of the pre-synthesized nanoparticles is still in its infancy. It deserves to be extended to other nanoparticles.

In this article, we are interested in zirconium oxide (ZrO_2) nanocrystals. Several authors, among them Professor Giancarlo Righini, have demonstrated the potential of this nanocrystal to be a very promising co-dopant for rare-earth ions in silica glass for optical applications [24,25]. With a wide bandgap of 5 eV and a low phonon energy of 470 cm^{-1} [26–28], ZrO_2 effectively enhances radiative transitions in rare-earth-doped nanocrystals. It is also notable for its high refractive index (n = 2.15 at 633 nm) which can induce strong light scattering for sensors [28].

Several studies are related to the presence of ZrO_2 nanocrystals in optical fibers made by the MCVD (Modified Chemical Vapor Deposition) process. They all dealt with phase separation mechanism to form those nanocrystals. Based on a zirconia sol used as doping solution, scanning electron microscopy (SEM) images reveal the presence of nanoparticles in the preform, but their composition and structure were not characterized [29]. In another study, tetragonal ZrO_2 phase was identified by X-ray diffraction in a sol-gel preform [30]. The characterization of the nanoparticles in the fiber was only reported in three articles to the best of our knowledge. Based on a sol-gel approach, monoclinic zirconia phase was confirmed by X-ray diffraction in fiber [28]. Nanoparticles were also observed in the fiber core by transmission electron microscopy (TEM) when Zr, Y, Al and Yb chlorides were dissolved in the doping solution. However, their composition is not pure ZrO_2 as they also contain Al, Ge and Yb elements [31]. Zirconium, yttrium and erbium elements were reported to be dominant in the oxide nanoparticles when Al, Zr, Er and Y chlorides are used [32].

Here, we propose an alternative approach based on the MCVD and the direct doping of the porous layer with pre-synthesized ZrO_2 nanocrystals dispersed in the doping solution. Regarding the high melting temperature of ZrO_2 (about 2680 °C [33]), such nanocrystals are usually considered to be preserved all along the fabrication process. However, in our case, nanocrystals are embedded in silica matrix. The phase diagram of the SiO_2–ZrO_2 system reveals that both phases can mix to form $ZrSiO_4$ at temperature up to 1680 °C and a single homogeneous liquid (i.e. a complete dissolution of ZrO_2 crystals) at temperature lower than 2000 °C (temperature reached during the fabrication of both the preform and the fiber) [34]. Based on these considerations, we focused our attention on the potential evolution of the nanocrystals all along the fabrication process, from the pre-synthesized nanocrystals up to the fiber. Based on SEM, TEM and EDS (Energy Dispersive X-ray spectroscopy) analyses, we demonstrate that ZrO_2 nanocrystals are present both in the preform and the fiber. This opens new perspective to prepare fiber with ZrO_2 nanocrystals.

2. Experimental

2.1. Preform and fiber fabrication

Our aim in this study is to follow the evolution of ZrO_2 nanoparticles within the silica matrix throughout the manufacturing process of optical fiber. Firstly, the preform was fabricated using the Modified Chemical Vapor Deposition (MCVD) process. A porous germanium-doped silica layer was deposited at 1630 °C inside high-purity silica tube provided by Heraeus. Flow rate of oxygen was 50 cc/min in both $SiCl_4$ and $GeCl_4$ bubblers. The outer and inner diameters of the tube were 20 mm and 17 mm, respectively. The tube containing the porous layer was then immersed in a suspension of monoclinic ZrO_2 nanoparticles (40 nm in size, US Research Nanomaterials, Inc) dispersed in ethanol under magnetic stirring at 500 rpm for 1 h. This suspension was prepared by suspending 3 g of ZrO_2 nanoparticles in 45 mL of ethanol (concentration of 0.67 g/L). It is important to highlight that, while the use of an ultrasound bath can be effective in preventing nanoparticle aggregation, this method was not employed as it tends to remove the porous layer from the substrate tube. After removing the doping solution, the resulting impregnated porous layer was dried on the MCVD lathe at approximately 1000 °C under oxygen flow. Subsequently, the porous layer was gradually densified by increasing the temperature (from 1500 °C to 1900 °C). The tube was then collapsed at a temperature of 2000 °C to form the final glass rod (the preform). The obtained preform (1 cm in diameter) shows a dense white coloration of its core, attributed to the presence of nanoparticles-induced light scattering.

Finally, this preform was drawn into a 125-μm fiber in a fiber drawing tower at 1950 °C under standard conditions.

2.2. Electron microscopy analyses

To detect the presence of nanoparticles in both the preform core and the optical fiber core, a section (2–3 mm thick) was cut from the end of the preform and polished on one side, while the optical fiber was cleaved. Samples were carbon-coated prior being analyzed using a Tescan Vega3 XMU scanning electron microscope (Tescan France, Fuveau, France) equipped with an Oxford X-MaxN 50 EDS detector (Oxford Instruments, Abingdon, U.K.). For detailed morphological and structural analyses, transmission electron microscopy (TEM) analyses were performed using a Titan SPECTRA 200 transmission electron microscope operating at 200 kV equipped with a cold FEG (Field emission Gun) and a Cs aberration probe corrector together with 2 large EDS (Energy dispersive X-ray spectroscopy) detectors presenting a high sensibility corresponding to a solid angle of 1.8 sr. All the analyses were performed using a probe convergent semi-angle of 29.4 mrad and a collection angle between 109 and 200 mrad allowing STEM-HAADF (Scanning Transmission electron microscopy-High angle annular dark field imaging mode). For the chemical analysis done using EDS within the STEM-HAADF imaging we considered silicon as element of interest with Kα = 1.7400 KeV ionization edge, O with Kα = 0.5230 KeV ionization edge and Zr with Lα = 2.0423 KeV ionization edge. The total probe current for this analysis was set to about 85 pA. To facilitate the analysis, the ZrO_2 NPs were directly deposited on TEM copper grids after dispersion within ethanol.

To access the characteristics of the ZrO_2 NPs within the preform prior to the electron microscopy analyses the sample was carefully cut in order to isolate the fiber core, minimizing the inclusion of the cladding. The end of the sample was then ground using an agate mortar, and the resulting powder was dispersed in 96 % ethanol. A drop of this suspension was then added on a TEM copper grid. For the characterization of the ZrO_2 NPs within the core of the optical fiber the focused Ion Beam (FIB) preparation technique was used for preparing a thin lamella taken in specific area previously identified by performing SEM observations.

3. Results

3.1. Characterization of the commercial ZrO_2 nanoparticles

To form ZrO_2-doped preforms, glass tube was impregnated with spherical crystalline ZrO_2 nanoparticles, about 40 nm sized, provided by US Research Nanomaterials, Inc. To confirm their size, structure, morphology and composition, STEM analyses were performed on several assemblies of ZrO_2 NPs. The STEM-HAADF images illustrated in Fig. 1a allow us to confirm the size of the NPs which is about 40 nm with a size distribution between 30 and 50 nm estimated by counting 100 nanoparticles. The chemical analysis illustrated in Fig. 1b and c, performed using the STEM-EDS imaging mode allowed us revealing that the nanoparticles are mainly composed of Zr and O, with 70.03 ± 2.69 at% of Zr and 29.97 ± 2.69 at% of O, in accordance with the ZrO_2 composition given by the provider: The impurities in the ZrO_2 nanoparticles are less than 1 %, with a composition of $ZrO_2 + HfO_2 > 99.9$ % and $ZrO_2 > 99$ %. From the STEM-HAADF images we can observe that the morphology of the ZrO_2 NPs presents some facets. Moreover, closer analyses done at higer magnification (Fig. 1d–f) on the NPs allowed us evidencing the NPs crystalline structure.

In the Fast Fourier Transform taken on the selected area on the NPs, the interplanar spacing of $d_1 = 0.300$ nm corresponds to the (−1 -1 1) plane (Fig. 1e–f). According to the JCPDS 37–1484 database, this result is consistent with the monoclinic phase of ZrO_2.

3.2. Characterization of the ZrO_2 NPs in the preform core

Fig. 2 presents SEM images of the transverse section of the preform sample. As can be observed, the core exhibits a distinctive starburst shape, a structural feature that has been previously reported in germanosilicate preforms prepared by the MCVD process [35]. This phenomenon has been attributed to a higher viscosity of the core layer compared to that of the silica cladding. The difference in viscosity between the two glasses can result in the formation of this starburst shape during the collapse stage. In our preform, the core layer was doped with ZrO_2 NPs which may have contributed to an increase in the core glass viscosity. Indeed, it has been reported that the presence of nanocrystals induces an increase in the effective viscosity of the glass [36].

Average concentration of Zr element was determined by SEM-EDS measurement. From these analyses we observed that its concentration is higher in the center of the core (7 wt%, 1.5 at%) than close to the core-cladding interface (less than 1 wt%, 0.12 at%). A more detailed analysis of the core composition is presented in the next section.

To access more precise information concerning the composition and the structure of the ZrO_2 NPs after their impregnation within the preform we further analyzed them using high-resolution STEM-HAADF and STEM-EDS elemental mapping. Fig. 3 presents this detailed analysis in Fig. 3a a STEM-HAADF image illustrating a part of the preform core containing the ZrO_2 NPs homogeneously dispersed within the preform matrix mainly composed of silica (SiO_2). Contrary to the commercialized ZrO_2 NPs which present a facets morphology, the ZrO_2 NPs present within the preform presents a more spherical morphology with 2 well separated sizes, smaller one up to 8 nm or larger one up to 40 nm (Fig. 3a). From the HR-STEM image illustrated in Fig. 3b we were able to reveal information about the crystalline structure. From the FFT (Fig. 3c) could estimate an interplanar spacing $d_2 = 0{,}310$ nm for the (−1, −1, 1) plane, indicating that the monoclinic phase after the impregnation is preserved (Fig. 3b and c).

An important question that arises at this stage of analysis concerns the chemical composition of the formed ZrO_2 nanoparticles. Given their characteristics significantly different, i.e smaller size and spherical morphology, compared to commercial ZrO_2 nanoparticles, we aimed to determine whether this modification is related to the incorporation of silicon atoms contained within the preform matrix. Elucidating this information is highly challenging, as most of the ZrO_2 nanoparticles are

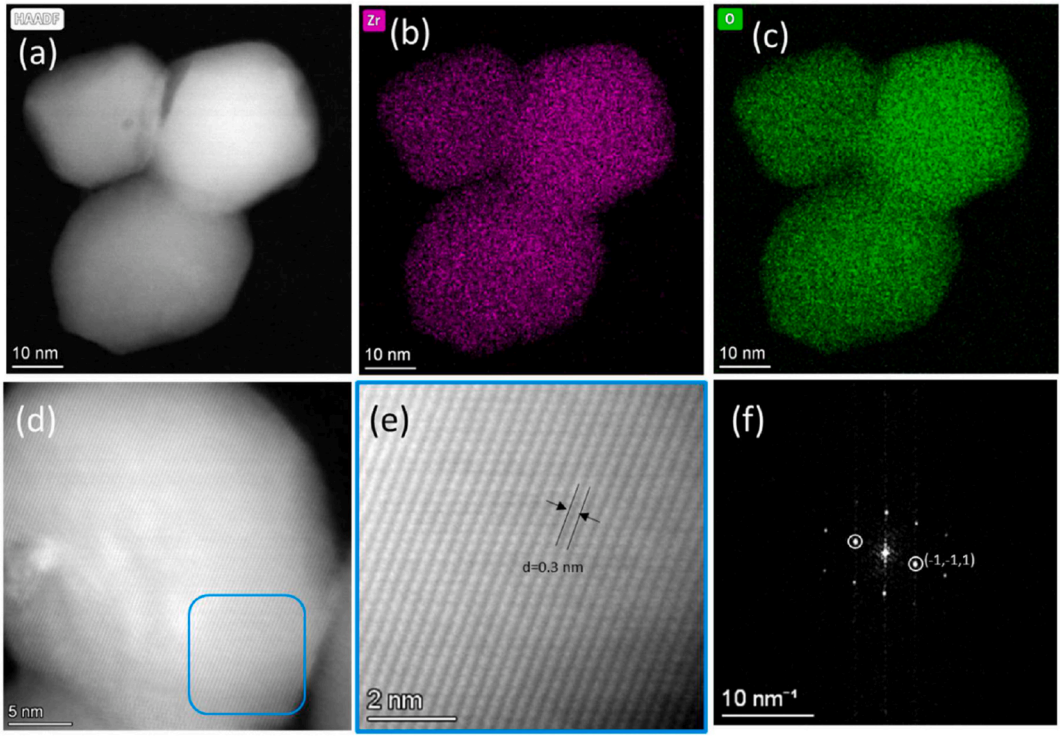

Fig. 1. (a) Image STEM-HAADF illustrating an assembly of ZrO_2 nanoparticles presenting a faceted morphology and its corresponding STEM-EDS chemical analyses with in (b) the Zr elemental map and in (c)the oxygen elemental map; (d) HR-STEM-HAADF image on a ZrO_2 NP with in (e) zoom on an area illustrating the NPs crystalline structure and (f)Fast Fourier Transform (FFT) of the area marked by the blue square in (d). (For interpretation of the references to color in this figure legend, the reader is referred to the Web version of this article.)

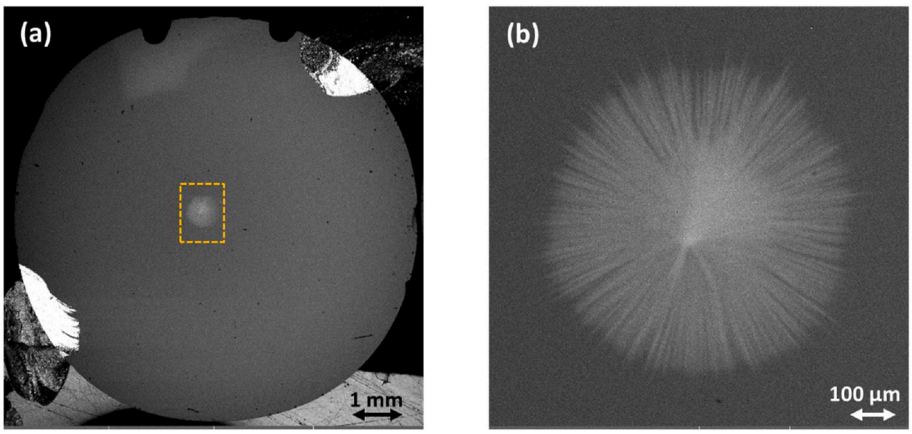

Fig. 2. SEM images of (a) the preform with (b) a close-up on the core.

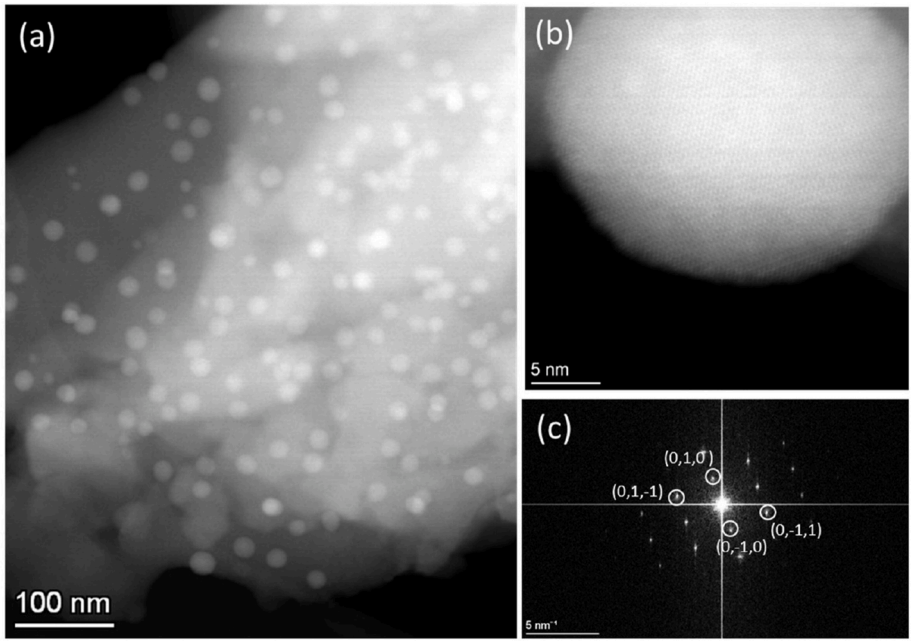

Fig. 3. (a) STEM-HAADF image of ZrO_2 nanoparticles within the preform core, (b) high magnification STEM-HAADF image on a unique ZrO_2 NP with in (c) its corresponding FFT illustrating its crystalline structure with $d_1 = 0.550$ nm corresponding to the (0, 1, 0) interplanar distance and $d_2 = 0.310$ nm corresponding to (−1, −1, 1) interplanar distance.

embedded within the silica preform matrix. Consequently, the chemical signal in an EDS elemental map will originate from both the matrix and the nanoparticles. Several areas containing both the ZrO_2 nanoparticles and the SiO_2 matrix were identified and analyzed by STEM-EDS chemical mapping (Fig. 4). A close elemental analysis on a single ZrO_2 NP, for which a small part was not embedded within the preform matrix, indicates a large difference in the silicon concentration. As can be seen in Fig. 4, the chemical analyses on a small area selected on the outer part of the nanoparticle shows concentration of 62.66 ± 3.16 atomic % O and 33.31 ± 3.27 atomic % Zr with a very small Si concentration about 4.04 ± 1.07 atomic % (Area 02, Fig. 4b and Table 1). This finding combined with the HR-STEM analysis, makes us advance that the ZrO_2 NPs in the preform core preserve their initial crystalline structure, i.e the monoclinic phase even if their morphology has undergone some modifications.

3.3. Characterization of the ZrO_2 nanoparticles in the fiber core

SEM images taken on different areas of the fiber along its transversal and longitudinal cross-sections are reported in Fig. 5. As can be observed, the ZrO_2 nanoparticles are dispersed in the central part of the core. According to the longitudinal cross-sectional image (Fig. 5b), the ZrO_2 NPs retained their initial spherical shape, and they don't undergo any elongation or fragmentation during the drawing process [18,37]. Information about the composition of the fiber core could also be obtained by performing SEM-EDS chemical analyses at different locations at the fiber surface marked in Fig. 5b. The corresponding concentrations are reported in Table 2. The highest concentration of Zr content corresponds to the area containing the nanoparticles (area 06 in Fig. 5b). This area contains a lower content of germanium. A lower concentration of germanium is commonly observed for the preform prepared with the MCVD process and it is attributed to the evaporation of this element during the collapse stage. Zr is detected in the central part of the core (where nanoparticles are observed) but also around this part (areas 05 et 07 in Fig. 5b). A lower concentration of Zr around the core may be detrimental to trigger the formation of ZrO_2 nanoparticles by phase separation. Or nanoparticles are too small to be detected by SEM.

To go further with the characterizations of the nanoparticles

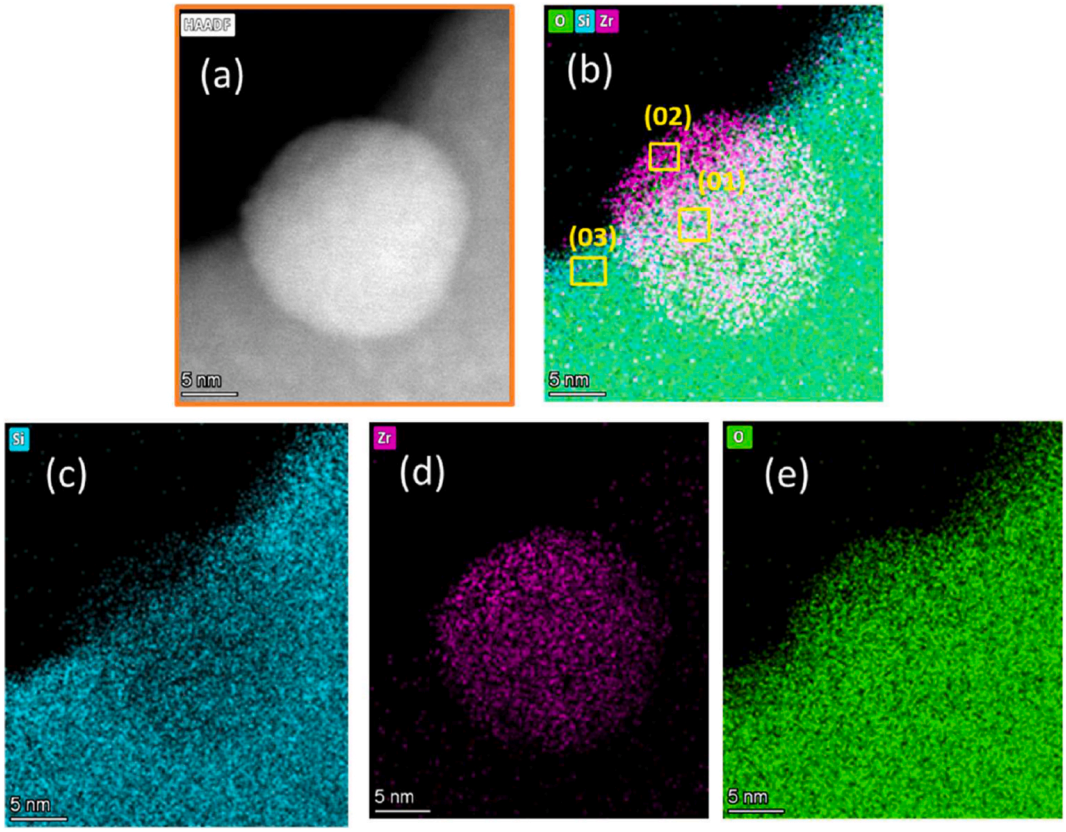

Fig. 4. (a) STEM-HAADF image of a 20-nm sized ZrO_2 NP for which a small part is emerging from the silica matrix and its corresponding STEM-EDS chemical analysis in (b) illustrating the distribution of Si, Zr and O elements within a chosen area represented in (c), (d) and (e) respectively.

Table 1
Concentration (in atomic %) of each element contained within the fiber core estimated from the STEM-EDS chemical analyses. The selected area number refers to Fig. 4b.

	O (atomic %)	Si (atomic %)	Zr (atomic %)
Area 01	61.39 ± 3.01	23.22 ± 3.46	15,39 ± 1.84
Area 02	62.66 ± 3.16	4.04 ± 1.07	33.31 ± 3.27
Area 03	51.91 ± 4.81	47.66 ± 4.85	0.43 ± 0.57

contained within the fiber core a thin cross-section lamella was prepared using the FIB preparation technique. Fig. 6 depicts a cross-sectional view of a TEM lamella, featuring a portion of the core fiber with ZrO_2 nanoparticles concentrated in the center. The fiber core is highlighted within a 3 μm-wide region.

Regarding the crystalline structure of the ZrO_2 NPs embedded within the fiber core, deeper analyses have been performed using electron diffraction analyses on a selected area of the FIB lamella containing several ZrO_2 NPs.

Fig. 7 displays an HR-STEM image of ZrO_2 NPs within the fiber matrix, along with zoomed-in view of different area highlighting their crystalline structure. The corresponding Fast Fourier Transform (FFT) pattern reveals the crystalline structure of corresponding NP with diffraction spots indicating the crystalline nature of the ZrO_2 NPs. These observations are further supported by Figs. SI–2.

Chemical analysis conducted using the STEM-EDS mode (Fig. 8) on the ZrO_2 nanoparticles embedded within the fiber core confirmed, as expected, that the nanoparticles are rich in Zr and O, while the surrounding matrix is predominantly composed of silica. As can be seen on the silicon elemental map, the silicon signal is decreasing at the ZrO_2 places.

A detailed analysis of the chemical maps was performed on ZrO_2 NPs

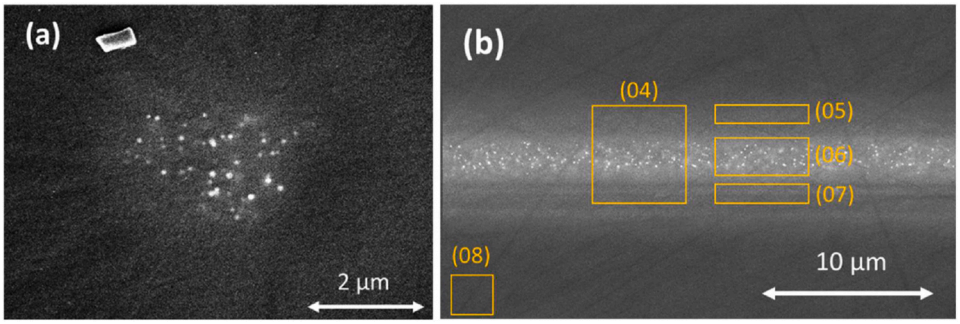

Fig. 5. SEM images illustrating a transverse (a) and a longitudinal (b) cross-section of the fiber containing the ZrO_2 NPs. The orange rectangles in (b) correspond to areas which have been chosen for the SEM-EDS chemical analyses; the Areas (04–08) marked in (b) correspond to EDS analyses discussed in the text and reported in Table 2. (For interpretation of the references to color in this figure legend, the reader is referred to the Web version of this article.)

Table 2
The concentration (in mol %) of each element contained within the fiber core measured by estimated from the SEM-EDS chemical analyses. The area number refers to Fig. 5b.

	Area 04	Area 05	Area 06	Area 07	Area 08[a]
SiO_2	97.24	98.05	96.34	97.72	100
ZrO_2	1.95	1.08	3.27	0.99	0
GeO_2	0.81	0.87	0.39	1.29	0

[a] Cl (0.14 wt%) was detected in this area only.

in two distinct areas (09) and (10) enabled precise determination of the atomic percentage of each element, with the corresponding values listed in Table 3. These results confirm that the nanoparticles are primarily composed of Zr and O (Fig. 9 and Table 3), Regarding silicon, analysis of the area (09) in its corresponding chemical map revealed a content less than 1 %, confirming that the NPs consist entirely as ZrO_2. In contrast, the matrix is characterized by a high concentration of silicon and oxygen, consistent with the expected composition for SiO_2 glass.

4. Discussion

The detailed morphological and structural characterization of the ZrO_2 NPs during the different steps reveals that they preserve their initial composition and crystalline monoclinic structure. However, these analyzes were carried out in cooled materials and do not allow us to conclude that the nanocrystals do not evolve at high temperatures during the different manufacturing phases.

One of the possible reactions between ZrO_2 and SiO_2 could lead to the formation of $ZrSiO_4$, a phase that is stable only at temperatures up to

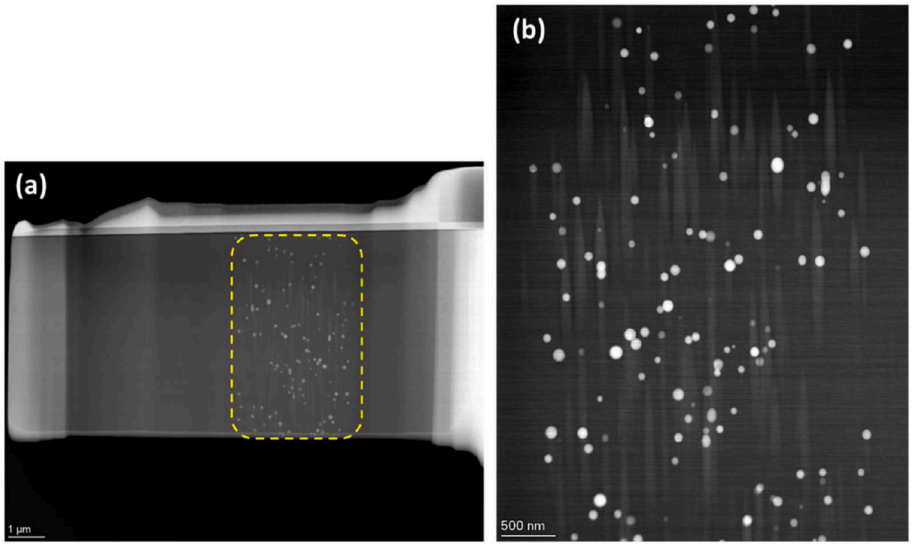

Fig. 6. low magnification STEM-HAADF of a cross-sectional lamella, featuring a portion of the core fiber with ZrO_2 nanoparticles concentrated in the center. The draw axis is along the vertical direction.; (b) a zoom on the center of the fiber highlighting the spherical morphology of the ZrO_2 nanoparticles (50–130 nm sized) located within the fiber core.

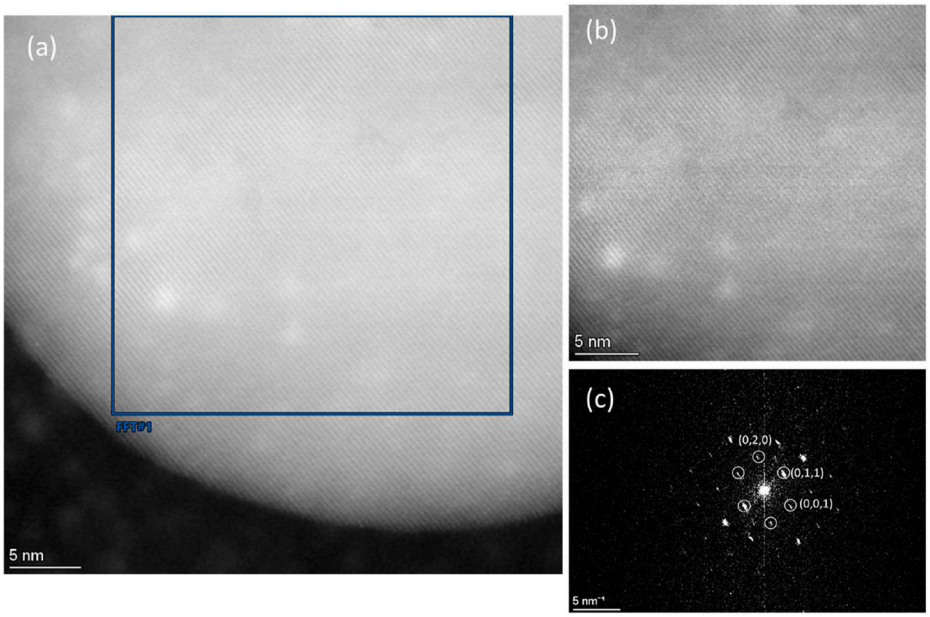

Fig. 7. (a) HR-STEM image of ZrO_2 NPs within the fiber matrix, (b) and (c) zoomed-in view of one area highlighting the crystalline structure of the NPs, and (c) FFT of the corresponding area, showing diffraction spots attributed to the crystalline structure of ZrO_2 nanoparticle.

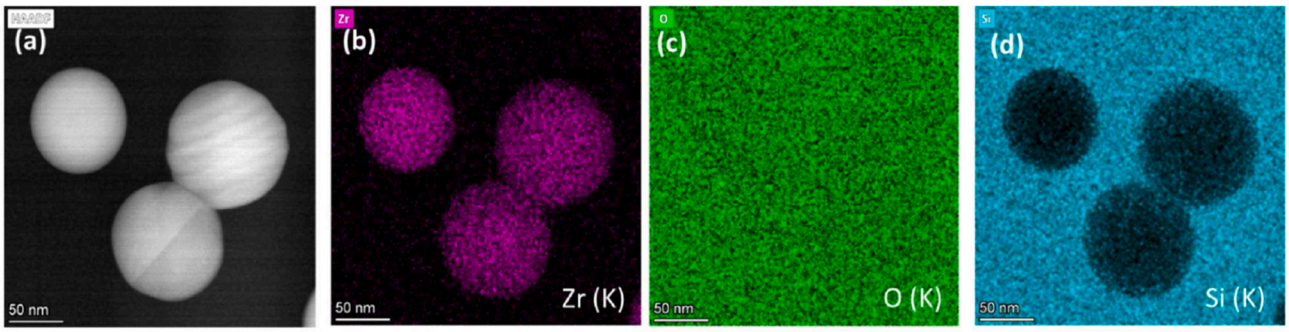

Fig. 8. (a) STEM-HAADF image on three selected ZrO_2 nanoparticles contained within the core fiber and the corresponding STEM-EDS elemental maps for Zr (b), O (c) and Si (d) elements.

Table 3
The concentration of each considered element (in atomic %) taken in two different areas (9) and (10) on the ZrO_2 NPs within the fiber core estimated from the STEM-EDS chemical analyses. The area number refers to Fig. 9d.

	O (atomic %)	Si (atomic %)	Zr (atomic %)
Area 09	68.49	0.94	30.57
Area 10	68.41	8.46	23.13

~1700 °C [34]. However, during both the MCVD process and fiber drawing, temperatures can reach 2000 °C or even more during the collapsing of the preform, exceeding the melting point of $ZrSiO_4$. Despite these extreme temperatures, the high-temperature steps persist for only a few minutes, whereas the decomposition of $ZrSiO_4$ microcrystals typically requires several hours of heat treatment at 1700 °C [34]. None of the analyzes revealed the presence of the $ZrSiO_4$ crystalline phase, neither in the preform nor in the fiber. The manufacturing process, as implemented, does not lead to the formation of $ZrSiO_4$, either by inhibiting the $SiO_2+ZrO_2 \rightarrow ZrSiO_4$ formation reaction, or by ensuring a sufficiently high temperature to melt this phase while avoiding its reformation when the temperature drops thanks to the fast-quenching operating during the drawing.

With an average ZrO_2 concentration of 3.27 mol% in the central part of the fiber core (Table 2, area 06), the phase diagram of the SiO_2–ZrO_2 binary system predicts the formation of a homogeneous liquid at 1726 °C [38].

It's worth noting that according to this phase diagram, the eutectic is obtained for a concentration of 5.6 mol% ZrO_2, very close to the concentration measured in the fiber. Given the temperatures involved during the manufacturing process, it is therefore possible that the initial ZrO_2 nanocrystals partly react with the silica matrix at high temperature. A melting of these crystals would explain the presence of Zr around the central part of the fiber core, in a zone without nanocrystals or very small ones (Fig. 5, areas 05 and 07). In addition, the melting of the smaller ZrO_2 nanocrystals would make it possible to supply the remaining nanocrystals, which would explain an increase in the average size of the nanocrystals during the manufacturing process.

5. Conclusion

In this work, ZrO_2 crystalline nanoparticles were successfully into silica matrix via solution impregnation, using the MCVD process within a glass tube. The evolution of these nanoparticles throughout the fabrication process, from preform synthesis to optical fiber drawing, was thoroughly investigated through various heat treatments.

Starting with 40-nm ZrO_2 nanocrystals, the resulting preforms

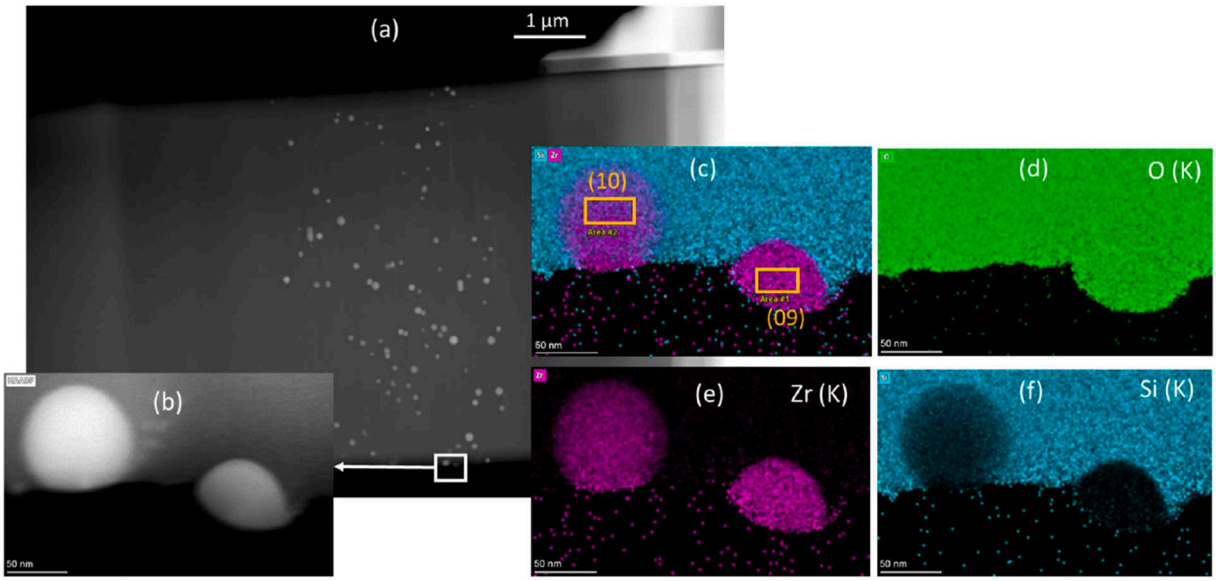

Fig. 9. (a) STEM-HAADF image of the cross-sectional FIB lamella illustrating the fiber region after its thinning using ion milling by PIPS, (b) showing an area with ZrO_2 NPs not embedded in the fiber matrix (c) STEM-EDS chemical analysis of two different areas (09) and (10) with the elemental maps of each considered elements, (d) O, (e) Zr and (f) Si marked by orange rectangles in area (c). (For interpretation of the references to color in this figure legend, the reader is referred to the Web version of this article.)

revealed the presence of spherical nanocrystals ranging in size from 8 to 40 nm. TEM diffraction confirmed that these nanoparticles retained their monoclinic ZrO_2 crystal structure, with no evidence of structural transformation or SiO_2–ZrO_2 phase formation during the MCVD process.

The fiber resulting from the preform drawing contained spherical crystalline nanoparticles ranging in size from 50 to 130 nm. The analysis revealed that there has been no structural alterations and that the ZrO_2 nanoparticles are monoclinic.

While the same nanocrystals are observed in the final fiber as the ones dispersed in the doping solution, we do not claim that ZrO_2 nanocrystals do not evolve all along the fabrication process. In particular, the change of their size could be explained by their partial melting as supported by the phase diagram.

These findings highlight the potential and the robustness of this approach to obtain nanocrystals in the as-drawn fiber (without additional heat-treatment), based on the JCVD process. Moving forward, the next step will be to investigate the luminescence properties of these ZrO_2 nanocrystals by doping them with rare-earth ions, further expanding their potential applications.

CRediT authorship contribution statement

Lilia Sennoun: Methodology, Validation, Formal analysis, Investigation, Resources, Writing – original draft, Writing – review & editing, Visualization, Funding acquisition. **Ileana Florea:** Methodology, Validation, Formal analysis, Investigation, Writing – review & editing, Visualization. **François Orange:** Methodology, Validation, Formal analysis, Investigation, Writing – review & editing, Visualization. **Michele Ude:** Methodology, Investigation, Resources, Writing – review & editing. **Peter Hesemann:** Conceptualization, Methodology, Validation, Formal analysis, Investigation, Resources, Writing – review & editing, Supervision. **Ahmad Mehdi:** Conceptualization, Methodology, Validation, Formal analysis, Investigation, Resources, Writing – review & editing, Supervision. **Wilfried Blanc:** Conceptualization, Methodology, Validation, Formal analysis, Investigation, Resources, Writing – original draft, Writing – review & editing, Visualization, Supervision, Funding acquisition.

Editor disclosure statement

Given his role as Editor for this journal, Wilfried Blanc had no involvement in the peer review of articles for which he was an author and had no access to information regarding their peer-review. Full responsibility for the peer-review process for this article was delegated to another Editor.

Declaration of competing interest

The authors declare the following financial interests/personal relationships which may be considered as potential competing interests: Wilfried Blanc reports financial support was provided by French National Research Agency. Lilia Sennoun reports financial support was provided by Algerian Government. If there are other authors, they declare that they have no known competing financial interests or personal relationships that could have appeared to influence the work reported in this paper.

Acknowledgements

The authors acknowledge the financial support from Algerian Government for the Algerian grant of excellence 2019 awarded to Lilia Sennoun.

This work was supported by the Nanoslim ANR-17-CE08-0002-05 project, granted by The French National Research Agency.

Appendix A. Supplementary data

Supplementary data to this article can be found online at https://doi.org/10.1016/j.optmat.2025.117015.

Data availability

Data will be made available on request.

References

[1] J.M. Ballato, If you can use silica, use silica, in: Fiber Lasers and Glass Photonics: Materials Through Applications IV, 2024, p. 43, https://doi.org/10.1117/12.3025728. SPIE, Strasbourg, France.

[2] B. Faure, W. Blanc, B. Dussardier, G. Monnom, Improvement of the Tm^{3+}:$^3H_4$ level lifetime in silica optical fibers by lowering the local phonon energy, J. Non-Cryst. Solids 353 (2007) 2767–2773, https://doi.org/10.1016/j.jnoncrysol.2007.05.025.

[3] P. Lu, N. Lalam, M. Badar, B. Liu, B.T. Chorpening, M.P. Buric, P.R. Ohodnicki, Distributed optical fiber sensing: review and perspective, Appl. Phys. Rev. 6 (2019) 041302, https://doi.org/10.1063/1.5113955.

[4] W. Blanc, Y. Gyu Choi, X. Zhang, M. Nalin, K.A. Richardson, G.C. Righini, M. Ferrari, A. Jha, J. Massera, S. Jiang, J. Ballato, L. Petit, The past, present and future of photonic glasses: a review in homage to the united nations international year of glass 2022, Prog. Mater. Sci. 134 (2023) 101084, https://doi.org/10.1016/j.pmatsci.2023.101084.

[5] A. Agnesi, G.P. Banfi, G.C. Reali, G.C. Righini, Nonlinear optical transmission in semiconductor-doped glasses, Proc. SPIE 1128, Glasses for Optoelectronics (1989) 256, https://doi.org/10.1117/12.961469.

[6] G.C. Righini, G.P. Banfi, V. Degiorgio, F. Nicoletti, S. Pelli, Semiconductor doped glasses: structural and waveguide characterization, Mater. Sci. Eng., B 9 (1991) 397–403, https://doi.org/10.1016/0921-5107(91)90061-Y.

[7] G. Fagherazzi, P. Riello, G.C. Righini, Structural characterization of Cd (se, S)-doped glasses, J. Non-Cryst. Solids 142 (1992) 63–69, https://doi.org/10.1016/S0022-3093(05)80007-9.

[8] S.N.B. Bhaktha, F. Beclin, M. Bouazaoui, B. Capoen, A. Chiasera, M. Ferrari, C. Kinowski, G.C. Righini, O. Robbe, S. Turrell, Enhanced fluorescence from Eu^{3+} in low-loss silica glass-ceramic waveguides with high SnO_2 content, Appl. Phys. Lett. 93 (2008) 211904, https://doi.org/10.1063/1.3037224.

[9] Y. Jestin, C. Armellini, A. Chiappini, A. Chiasera, M. Ferrari, C. Goyes, M. Montagna, E. Moser, G. Nunzi Conti, S. Pelli, R. Retoux, G.C. Righini, G. Speranza, Erbium activated HfO_2 based glass–ceramics waveguides for photonics, J. Non-Cryst. Solids 353 (2007) 494–497, https://doi.org/10.1016/j.jnoncrysol.2006.10.016.

[10] G. Alombert-Goget, C. Armellini, S. Berneschi, A. Chiappini, A. Chiasera, M. Ferrari, S. Guddala, E. Moser, S. Pelli, D.N. Rao, G.C. Righini, Tb^{3+}/Yb^{3+} co-activated silica-hafnia glass ceramic waveguides, Opt. Mater. 33 (2010) 227–230, https://doi.org/10.1016/j.optmat.2010.09.030.

[11] L. Zur, C. Armellini, S. Belmokhtar, A. Bouajaj, E. Cattaruzza, A. Chiappini, F. Coccetti, M. Ferrari, F. Gonella, G.C. Righini, E. Trave, A. Vomiero, F. Enrichi, Comparison between glass and glass-ceramic silica-hafnia matrices on the down-conversion efficiency of Tb^{3+}/Yb^{3+} rare Earth ions, Opt. Mater. 87 (2019) 102–106, https://doi.org/10.1016/j.optmat.2018.05.008.

[12] W. Blanc, D. Tosi, A. Leal-Junior, M. Ferrari, J. Ballato, Are low- and high-loss glass–ceramic optical fibers possible game changers? Opt. Commun. 575 (2025) 131300 https://doi.org/10.1016/j.optcom.2024.131300.

[13] W. Blanc, Z. Lu, T. Robine, F. Pigeonneau, C. Molardi, D. Tosi, Nanoparticles in optical fiber, issue and opportunity of light scattering, Opt. Mater. Express 12 (2022) 2635–2652, https://doi.org/10.1364/OME.462822 [Invited].

[14] P.A. Tick, Are low-loss glass–ceramic optical waveguides possible? Opt Lett. 23 (1998) 1904–1905, https://doi.org/10.1364/OL.23.001904.

[15] D. Tosi, C. Molardi, M. Sypabekova, W. Blanc, Enhanced backscattering optical fiber distributed sensors: tutorial and review, IEEE Sensors J 21 (2021) 12667–12678, https://doi.org/10.1109/JSEN.2020.3010572.

[16] W. Blanc, V. Mauroy, L. Nguyen, B.N. Shivakiran Bhaktha, P. Sebbah, B.P. Pal, B. Dussardier, Fabrication of rare earth-doped transparent glass ceramic optical fibers by modified chemical vapor deposition, J. Am. Ceram. Soc. 94 (2011) 2315–2318, https://doi.org/10.1111/j.1551-2916.2011.04672.x.

[17] V. Fuertes, N. Grégoire, P. Labranche, S. Gagnon, R. Wang, Y. Ledemi, S. LaRochelle, Y. Messaddeq, Engineering nanoparticle features to tune rayleigh scattering in nanoparticles-doped optical fibers, Sci. Rep. 11 (2021) 9116, https://doi.org/10.1038/s41598-021-88572-2.

[18] M. Vermillac, J.-F. Lupi, F. Peters, M. Cabié, P. Vennéguès, C. Kucera, T. Neisius, J. Ballato, W. Blanc, Fiber-draw-induced elongation and break-up of particles inside the core of a silica-based optical fiber, J. Am. Ceram. Soc. 100 (2017) 1814–1819, https://doi.org/10.1111/jace.14774.

[19] Z. Lu, T. Robine, M. Guzik, M. Bellec, D. Tosi, C. Molardi, F. Pigeonneau, W. Blanc, Shaping nanoparticles in optical fibers through thermal engineering, in: Fiber Lasers and Glass Photonics: Materials Through Applications III, 2022, p. 23, https://doi.org/10.1117/12.2620076. SPIE, Strasbourg, France.

[20] Z. Lu, N. Vakula, M. Ude, M. Cabié, T. Neisius, F. Orange, F. Pigeonneau, L. Petit, W. Blanc, $YbPO_4$ crystals in as-drawn silica-based optical fibers, Opt. Mater. 138 (2023) 113644, https://doi.org/10.1016/j.optmat.2023.113644.

[21] V. Fuertes, N. Grégoire, P. Labranche, S. Gagnon, N. Hamada, B. Bellanger, Y. Ledemi, S. LaRochelle, Y. Messaddeq, Cubic-shaped and rod-shaped YPO_4 nanocrystal-doped optical fibers: implications for next generation of fiber lasers, ACS Appl. Nano Mater. 6 (2023) 4337–4348, https://doi.org/10.1021/acsanm.2c05449.

[22] T. Cheng, M. Liao, X. Xue, J. Li, W. Gao, X. Li, D. Chen, S. Zheng, Y. Pan, T. Suzuki, Y. Ohishi, A silica optical fiber doped with yttrium aluminosilicate nanoparticles for supercontinuum generation, Opt. Mater. 53 (2016) 39–43, https://doi.org/10.1016/j.optmat.2016.01.018.

[23] M. Vermillac, H. Fneich, J.-F. Lupi, J.-B. Tissot, C. Kucera, P. Vennéguès, A. Mehdi, D.R. Neuville, J. Ballato, W. Blanc, Use of thulium-doped LaF_3 nanoparticles to lower the phonon energy of the thulium's environment in silica-based optical fibres, Opt. Mater. 68 (2017) 24–28, https://doi.org/10.1016/j.optmat.2016.11.042.

[24] F. Enrichi, M. Cassetta, N. Daldosso, E. Cattaruzza, P. Riello, R. Zairov, A. Vomiero, G.C. Righini, Effect of the crystal structure on the optical properties and Ag sensitization of Tb^{3+}/Yb^{3+} ions in silica-zirconia glasses and glass-ceramics, Ceram. Int. 49 (2023) 41064–41070, https://doi.org/10.1016/j.ceramint.2022.10.036.

[25] M. Isogai, A. Veber, M. Cicconi, T. Hayakawa, D. De Ligny, Devitrification behavior of sol-gel derived ZrO_2-SiO_2 rare-earth doped glasses: correlation between structural and optical properties, Ceramics 1 (2018) 274–286, https://doi.org/10.3390/ceramics1020022.

[26] T. López-Luke, E. De La Rosa, D. Sólis, P. Salas, C. Angeles-Chavez, A. Montoya, L. A. Díaz-Torres, S. Bribiesca, Effect of the CTAB concentration on the upconversion emission of ZrO_2:Er^{3+} nanocrystals, Opt. Mater. 29 (2006) 31–37, https://doi.org/10.1016/j.optmat.2006.03.032.

[27] R.R. Reddy, Y. Nazeer Ahammed, P. Abdul Azeem, K. Rama Gopal, T.V.R. Rao, Electronic polarizability and optical basicity properties of oxide glasses through average electronegativity, J. Non-Cryst. Solids 286 (2001) 169–180, https://doi.org/10.1016/S0022-3093(01)00481-1.

[28] G. Brasse, C. Restoin, J.-L. Auguste, S. Hautreux, J.-M. Blondy, A. Lecomte, F. Sandoz, C. Pedrido, Nanoscaled optical fibre obtained by the sol–gel process in the SiO_2–ZrO_2 system doped with rare Earth ions, Opt. Mater. 31 (2009) 765–768, https://doi.org/10.1016/j.optmat.2008.03.021.

[29] P. Vařák, J. Mrázek, W. Blanc, J. Aubrecht, M. Kamrádek, O. Podrazký, Preparation and properties of Tm-doped SiO_2 -ZrO_2 phase separated optical fibers for use in fiber lasers, Opt. Mater. Express 10 (2020) 1383–1391, https://doi.org/10.1364/OME.394068.

[30] P. Bulot, R. Bernard, M. Cieslikiewicz-Bouet, G. Laffont, M. Douay, Performance study of a zirconia-doped fiber for distributed temperature sensing by OFDR at 800 °C, Sensors 21 (2021) 3788, https://doi.org/10.3390/s21113788.

[31] A.V. Kir'yanov, M.C. Paul, YuO. Barmenkov, S. Das, M. Pal, S.K. Bhadra, L. E. Zarate, A.D. Guzman-Chavez, Fabrication and characterization of new Yb-doped zirconia-germano-alumino silicate phase-separated nano-particles based fibers, Opt. Express 19 (2011) 14823–14837, https://doi.org/10.1364/OE.19.014823.

[32] Y.-W. Lee, J.-S. Chang, S. Das, A. Dhar, M. Pal, M.C. Paul, J.-T. Lin, Y.-W. Jhang, Er^{3+}-doped nano-engineered yttria stabilized zirconia–alumino silicate fiber for efficient CW and mode-locked laser operation, IEEE Photonics J 8 (2016) 1–13, https://doi.org/10.1109/JPHOT.2016.2585924.

[33] C.J. Howard, R.J. Hill, B.E. Reichert, Structures of ZrO_2 polymorphs at room temperature by high-resolution neutron powder diffraction, Acta Crystallogr B Struct Sci 44 (1988) 116–120, https://doi.org/10.1107/S0108768187010279.

[34] A. Kaiser, M. Lobert, R. Telle, Thermal stability of zircon ($ZrSiO_4$), J. Eur. Ceram. Soc. 28 (2008) 2199–2211, https://doi.org/10.1016/j.jeurceramsoc.2007.12.040.

[35] P. McNamara, K.J. Lyytikainen, T. Ryan, I.J. Kaplin, S.P. Ringer, Germanium-rich "starburst" cores in silica-based optical fibres fabricated by modified chemical vapour deposition, Opt. Commun. 230 (2004) 45–53, https://doi.org/10.1016/j.optcom.2003.11.049.

[36] D. Di Genova, A. Zandona, J. Deubener, Unravelling the effect of nano-heterogeneity on the viscosity of silicate melts: implications for glass manufacturing and volcanic eruptions, J. Non-Cryst. Solids 545 (2020) 120248, https://doi.org/10.1016/j.jnoncrysol.2020.120248.

[37] M. Cabié, T. Neisius, W. Blanc, Combined FIB/SEM tomography and TEM analysis to characterize high aspect ratio Mg-silicate particles inside silica-based optical fibres, Mater. Char. 178 (2021) 111261, https://doi.org/10.1016/j.matchar.2021.111261.

[38] W.C. Butterman, W.R. Foster, Zircon stability and the ZrO_2-SiO_2 phase diagram, Am. Mineral. 52 (1967) 880–885.